Transport of bubbles in square microchannels

Thomas Cubaud and Chih-Ming Ho
Mechanical and Aerospace Engineering Department, University of California at Los Angeles, 420 Westwood Plaza, Los Angeles, California 90095

(Received 24 February 2004; accepted 16 September 2004; published online 5 November 2004)

Liquid/gas flows are experimentally investigated in 200 and 525 μm square microchannels made of glass and silicon. Liquid and gas are mixed in a cross-shaped section in a way to produce steady and homogeneous flows of monodisperse bubbles. Two-phase flow map and transition lines between flow regimes are examined. Bubble velocity and slip ratio between liquid and gas are measured. Flow patterns and their characteristics are discussed. Local and global dry out of the channel walls by moving bubbles in square capillaries are investigated as a function of the flow characteristics for partially wetting channels. Two-phase flow pressure drop is measured and compared to single liquid flow pressure drop. Taking into account the homogeneous liquid fraction along the channel, an expression for the two-phase hydraulic resistance is experimentally developed over the range of liquid and gas flow rates investigated. © *2004 American Institute of Physics*.
[DOI: 10.1063/1.1813871]

I. INTRODUCTION

Multiphase flow occurs in many operations in the chemical, petroleum, and power generation industries (such as nuclear power plants and micro-fuel cells). Unlike large-scale systems, gas bubbles can present significant problems in microfluidic systems by disturbing and eventually blocking the flow. Interactions on the boundaries between gas, liquid, and solid introduce nonlinearity and instabilities. Understanding how bubbles affect the flow resistance in microchannels is, besides its fundamental aspect, a concern of determining the pumping or energy requirement for portable microfluidic devices where two-phase flow is involved such as in a microdirect methanol fuel cell.[1]

When the size h of a channel is sufficiently small so the Bond number Bo is smaller than unity, gravitational effects are likely to be small. In a square microchannel, when the bubble size d is larger than h, gas and liquid are neutrally buoyant and the cross section of the liquid-air interface possesses symmetries with respect to the center axis of the channel. While most of the two-phase flow literature reports experiments conducted with a complete wetting fluid, wetting often takes place either on heterogeneous surfaces or with contaminant preventing a complete wetting of the system and leading to the formation of a contact line. The contact angle has been shown to have a significant effect on two-phase flow in circular capillary.[2]

The conditions for bubble displacement through constricted polygonal capillaries were studied for a wetting fluid.[3–5] The shape of a meniscus inside an N-sided regular polygonal capillary depends on N and on the contact angle θ.[6,7] When $\theta < \pi/N$, the gas does not fill the entire polygon cross section. In the case of a square section, for $\theta < \pi/4$, liquid fills the wedges and gas fills the center. In a static condition and for a partially wetting liquid ($\theta > 0$), a contact line between liquid, gas, and solid is energetically privileged. When liquid and gas are flowing, the situation becomes rather complex because of dynamic contact angles ($\theta \sim \mathrm{Ca}^{1/3}$ where the capillary number $\mathrm{Ca} = \eta V/\gamma$ with η the viscosity, V the velocity, and γ the liquid/gas surface tension) and hysteresis.

Liquid/gas and liquid/liquid flows in microchannels have received an increasing experimental interest.[8–10] Different models have been proposed to predict the pressure drop across a bubble train in a square capillary[5,11–13] but, so far, no systematic experimental studies were performed taking into account the flow patterns. Interaction of gas and liquid phases in small channels often results in pressure and void fraction fluctuations.[14–16] Fluctuations affect the hydraulic resistance of the channel and average density of the mixture.

The objective of this work is to understand the conditions necessary to purge gas bubbles from square microchannels. We first discuss how liquid and gas are mixed in a cross-shaped section in a way to produce a steady and homogeneous flow in a microfluidic device. The two-phase flow map and the transition lines between flow regimes are drawn for 200 and 525 μm square microchannels. Over the range of liquid and gas flow rates investigated; the flow map remains the same regardless of channel size. Bubble velocity was measured and was found to be equal to the average mixture velocity. The apparent liquid fraction is compared to the homogeneous liquid fraction and the slip ratio between the liquid and the gas velocity is shown to monotonically increase with the mixture velocity. Flow patterns and their characteristics are then individually discussed. Because of the small channel size, wettability effects play an important role in the system. Wedging and dry flows are described as specific to noncircular partially wetting capillaries. These flows correspond to local or global dry out of the channel walls by bubbles. Finally, the pressure drop is measured from a single liquid flow to a single gas flow for different flow rates. Taking into account the homogeneous liquid fraction along the channel, expressions for the two-phase hydraulic resistance are experimentally developed when the liquid is

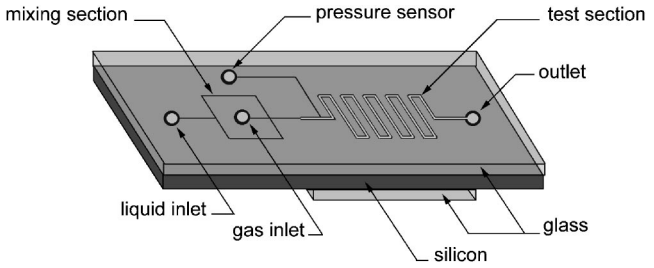

FIG. 1. Two-phase flow microchannel module: mixing section (50 μm square channel), test section (200 or 525 μm square channel).

mostly pushing the bubbles (high liquid fraction) and when liquid is mostly flowing in the corners (low liquid fraction).

II. EXPERIMENTAL SETUP

A. Microchannels fabrication

Channels are made with glass and silicon using microfabrication techniques.[17] Channel masks are printed in positive with a high-resolution printer on transparent paper for lithography. Photoresist is spin coated on a 10 cm double-sided polished silicon wafer. The wafer is then exposed to UV light through the mask. The parts of the resin layer exposed to UV light are removed by immersion in a developer bath. Channels are etched at different depths using deep reactive ion etching (DRIE). The sealing is made with Pyrex glass using anodic bonding, providing optical access for flow analysis. Flexible tubes are glued with epoxy on gas and liquid inlets and on the pressure sensor inlet.

Figure 1 shows a typical channel module. Channels are composed of two parts: a mixing section (50 ± 5 μm square channel) and a test section (200 ± 10 or 525 ± 10 μm square channel). A 50 μm square channel is connected to the main channel to allow pressure measurements. Experiments were conducted using de-ionized (DI) water and air. As channels were partially wetting, contact angle hysteresis was measured using DI water droplets on progressively tilted surfaces. Advancing and receding contact angles were measured on glass and on DRIE silicon just before the droplet started moving. The advancing contact angle on glass is $\theta_{a,glass}=25\pm1°$ and the advancing contact angle on DRIE silicon is $\theta_{a,silicon}=9\pm1°$. The receding contact angle for both glass $\theta_{r,glass}$ and $\theta_{r,silicon}$ were slightly above 0°. Dewetting phenomena were observed in the experiments confirming the nonstrictly zero receding contact angles.

B. Apparatus

A schematic diagram of the experimental apparatus is shown in Fig. 2. Liquid is injected into the channel from a reservoir, the pressure of which is adjustable with a miniature regulator. The liquid flow rate Q_L is measured at the channel inlet with a liquid volumetric flow meter (from 0 to 1 ml/min). Gas is coming from a compressed air tank, the pressure of which is also adjustable with a miniature regulator. Air flow rate Q_G is measured with gas mass flow meters (from 0 to 100 ml/min). Mass flow meters determine the volumetric flow rate at the channel outlet based on

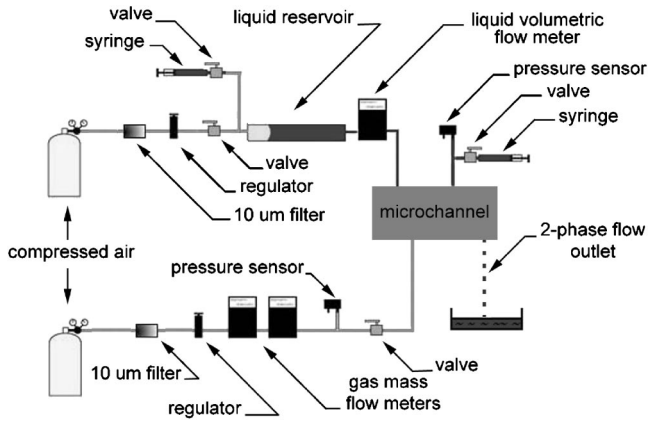

FIG. 2. Schematic of the experimental apparatus.

the viscosity of the air at the measured temperature. The pressure inside the test channel is measured with a differential pressure sensor ranging from 0 to 1, 5, or 15 psi depending on the flow rate. Before each measurement, the pressure sensor channel is flushed with water to remove all trapped air pockets. After each change of the gas inlet pressure, the system was allowed to reach a steady state. The steady state is defined when pressure sensors, flow meters, and bubble distribution are stationary. The measured pressure is averaged over 1000 points during 20 s. The liquid inlet pressure was limited to 50 psi ($\approx$3.4 atm). Because of the large pressure drop in the mixing channel section, limiting the range of liquid flow rate in the main channel, the maximum two-phase pressure drop measured in the test section presented in this paper is about 9 psi ($\approx$0.6 atm) for the dry flow, so that compressibility effects of gas are not significant since flow patterns and bubble size are uniformly distributed along the channels. In that case, a linear pressure distribution along the channel is assumed.[16]

A pressurized liquid reservoir was chosen instead of a mechanical syringe pump to allow the system to reach steady states. The channel outlet is permitted to vent directly into the atmosphere. A high-speed camera (10 000 frames per second) used with a 60 mm lens mounted on an extension tube is set above the channel to allow flow analysis. As channels are transparent, the light source (fiber light) is placed at the other side of the channels.

III. MIXING SECTION

Properly introducing gas bubbles is an important step in producing a two-phase flow pattern. We micromachined an effective small mixing section. Well-defined bubbles in a wide range of sizes can be produced as a function of liquid and gas flow rates. Figure 3 shows an example of liquid/gas mixing section in 100 μm square channels. Liquid and gas are mixed in a straight cross with three inlets and one outlet. The gas is coming from the center channel *A* and forms an elongated bubble pinched by the liquid coming from the sides (channels *B* and *C*). Two-phase flow occurs when gas and liquid flow through the outlet channel *D*. Micromachining allows channels *B* and *C* to be made perfectly symmetric in length and size so that, as they are connected to the same

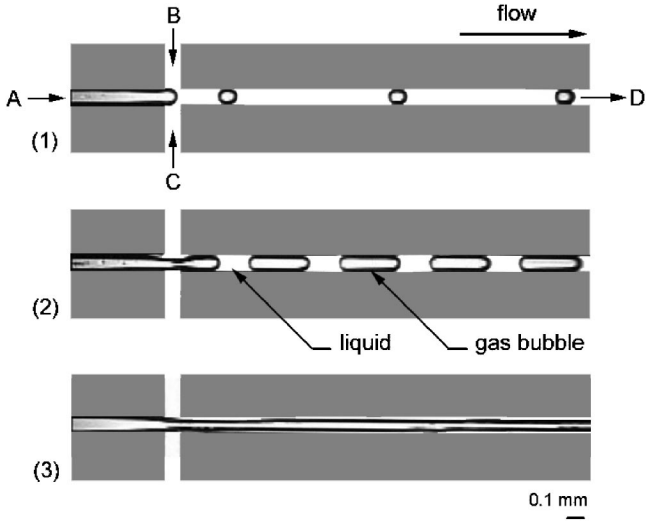

FIG. 3. Example of cross-shaped mixing section in 100 μm square channels: (a) gas inlet, (b) and (c) liquid inlets, and (d) two-phase flowing towards test section. (1) and (2) wedging flow, (3) annular flow.

liquid inlet, the liquid flow rate and pressure are identical in each of the channels. Because of the square channel symmetries, bubbles flow "naturally" in the center of the channel. The cross shaped was chosen to produce a steady uniform flow. This production technique of monodisperse bubbles presents some similarities with a capillary flow focusing technique.[18] In our geometry, the minimal size of bubbles is about the size of the channel. In these experiments, this mixing system is used as an effective way to produce two-phase flows in microdevices.

IV. TWO-PHASE FLOW MAP

Two-phase flows are distributed into several distinct flow patterns depending on the liquid and gas flow rates and fluid and channel properties. Five main flow regimes were observed in the partially wetting square microchannels: bubbly, wedging, slug, annular, and dry flows (see Fig. 4). Flow patterns are described in Sec. V. Besides differences in definition of flow patterns, some typical regimes observed in larger channels such as stratified, churn, or mist flows[19–21] were not observed in our channels within the range of laminar flow rates investigated.

Figure 5 shows the flow map and the transition lines between flow regimes for 200 and 525 μm channels. Liquid superficial velocity ($J_L = Q_L/A$, where A is the cross-section area) is plotted against gas superficial velocity ($J_G = Q_G/A$). Each set of experiments is conducted maintaining a constant liquid inlet pressure while gradually increasing the gas inlet pressure. The liquid flow rate Q_L then decreases because of the increase of the hydraulic resistance of the channel. Flow regime transitions are determined by visualization and examination of pressure drop data (see Sec. VI). Transitions between regimes are predictable as a function of liquid and gas flow rates. For both 200 and 525 μm channels, transitions between each regime occur for fixed values of the homogeneous liquid fraction α_L defined as

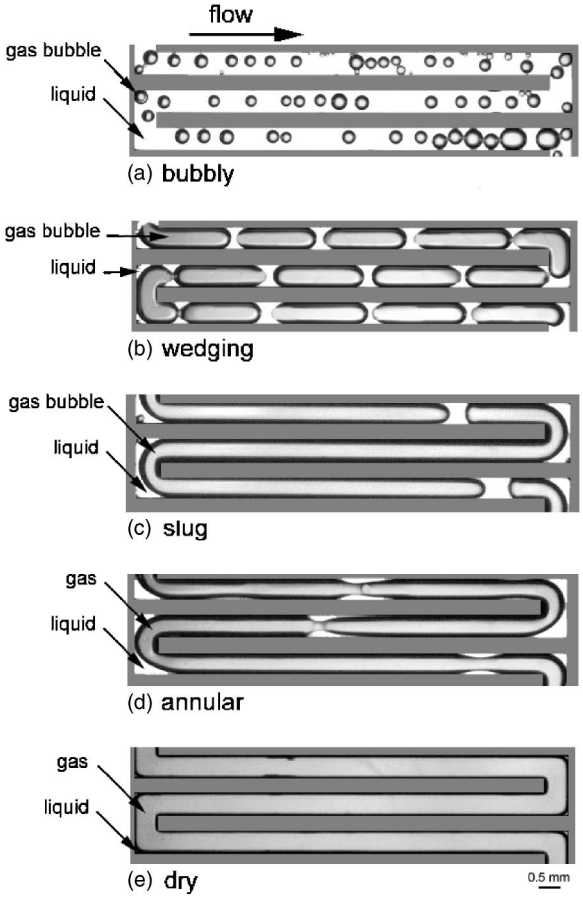

FIG. 4. Flow patterns from high to low liquid fraction α_L.

$$\alpha_L = \frac{Q_L}{Q_L + Q_G}. \tag{1}$$

The bubbly/wedging transition is for $\alpha_L \approx 0.75$; the wedging/slug transition is for $\alpha_L \approx 0.20$; the slug/annular transition is for $\alpha_L \approx 0.04$; and the annular/dry transition is for $\alpha_L \approx 0.005$, as can be seen in Fig. 5. While other transitions are smooth, the wedging/slug transition presents some hysteresis if the gas flow rate is increased or decreased. For $\alpha_L \approx 0.20 \pm 0.01$, the system is metastable, switching from a state to another at the same liquid and gas inlet pressure.

Over the range of flow rates investigated, because surface tension is predominant, transitions in square microchannels are not dependent on the channel diameter. This case is different from the case of macrochannels and minichannels (when $h > 1$ mm) where differences in the relative effects of gravitational, shear, and surface tension forces cause the transitions to be dependent on the channel diameter.[22] For a square channel, the hydraulic diameter is equal to the channel width h. Experiments in triangular microchannels pointed out the relevance of sharp edges in flow regime transitions.[23]

A. Bubbles velocity

For bubbly, wedging, and slug flows, the bubble velocity V_B is measured from processing consecutive images taken with a high-speed camera at 10 000 frames per second. For annular and dry flows the term "bubble" cannot be defined

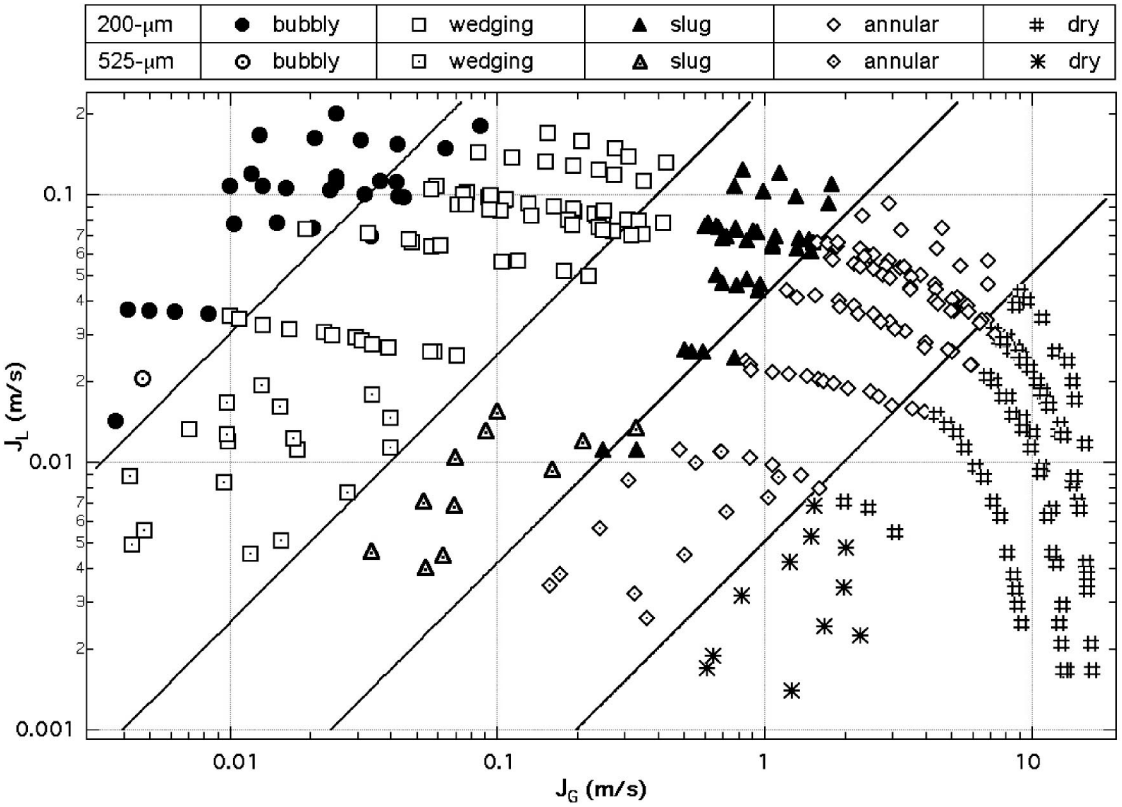

FIG. 5. Flow pattern map for horizontal flow in 200 and 525 μm square channels, air-water.

nor can the velocity be optically measured. For different homogeneous liquid fractions α_L, Fig. 6 compares the measured bubble velocity V_B to the average superficial velocity J, defined as the sum of the liquid and the gas superficial velocities:

$$V_B \approx J_L + J_G = J. \tag{2}$$

Over the range of measured velocities (from 0.01 to 1 m/s), the bubble velocity V_B can be assimilated to the average superficial velocity J. This result suggests that there is no corner flow. Contrary to circular channels,[24] no characteristic drift velocity between bubbles and the average speed of the fluid was measured in the present investigation. In studies using circular channels, as the channel diameter shrinks, drift velocity is reduced[21] and removed under microgravity conditions due to lack of buoyancy between liquid and gas.[25]

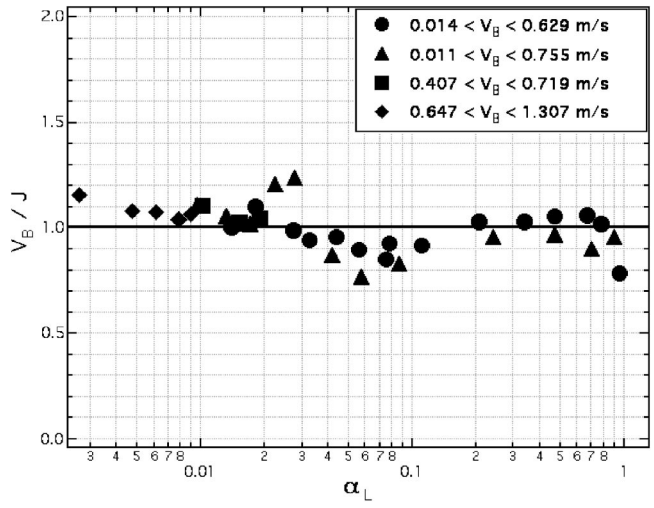

FIG. 6. Comparison of the bubble velocity V_B (measured by image processing) with the average superficial velocity J (measured with liquid and the gas flow meters) as a function of the homogeneous liquid fraction α_L for different initial conditions (h=525 μm).

B. Void fraction measurement

From image processing, the apparent time-averaged void fraction ε_G is calculated. Time-space diagrams are created from movies with a line plotted normal to the channel. For each liquid and gas flow rate, a composite image is created where the x coordinate corresponds to the channel width h and the y coordinate corresponds to the time t [Fig. 7 (left)]. As the liquid/air interface possesses symmetries with respect to the center axis of the channel [Fig. 7 (right)], ε_G is calculated as follows:

$$\varepsilon_G = \frac{\frac{\pi}{4}\sum d_t^2 + \sum (2l_t h - l_t^2)}{Th^2}, \tag{3}$$

where $d_t = 2r$ is the diameter of the curved interface, h is the height (and width) of the channel, l_t is the width of the core gas in "contact" with the walls, and $T = \Sigma t$ corresponds to the time of acquisition. Except for the bubbly flow (where $l_t = 0$), the liquid film between the gas and the center of the walls is neglected in the calculation of the total liquid volume be-

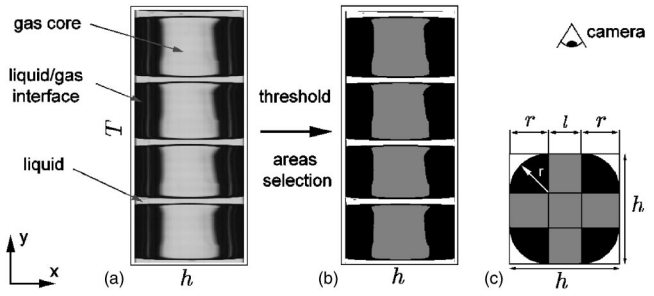

FIG. 7. Image processing to calculate the apparent void fraction ε_G. (a) Part of a raw time-space diagram (wedging flow), (b) threshold and area identified time-space diagram, (c) characteristic symmetries of a channel cross section.

cause it is negligible compared to the liquid volume in the corners. The apparent liquid fraction ε_L is simply defined as

$$\varepsilon_L = 1 - \varepsilon_G. \tag{4}$$

Figure 8 shows the relation between the apparent liquid fraction ε_L and the homogeneous liquid fraction α_L. Transitions between flow regimes are shown by straight vertical lines. Deviation from a linear relationship between ε_L and α_L occurs from the slug flow for $\alpha_L < 0.02$. Kolb and Cerro[26] showed the transition from an axisymmetrical to a symmetrical semi-infinite bubble profile in square channels when the capillary number Ca increases. This behavior results in an increase of the liquid fraction with the gas flow rate. The fact that the apparent void fraction α_L does not increase monotonically with Ca is specific to polygonal channels.

From the calculation of the apparent liquid and void fractions, the slip ratio S between liquid and gas can be defined as

$$S = \frac{V_G}{V_L} = \frac{J_G}{J_L}\frac{\varepsilon_L}{\varepsilon_G}. \tag{5}$$

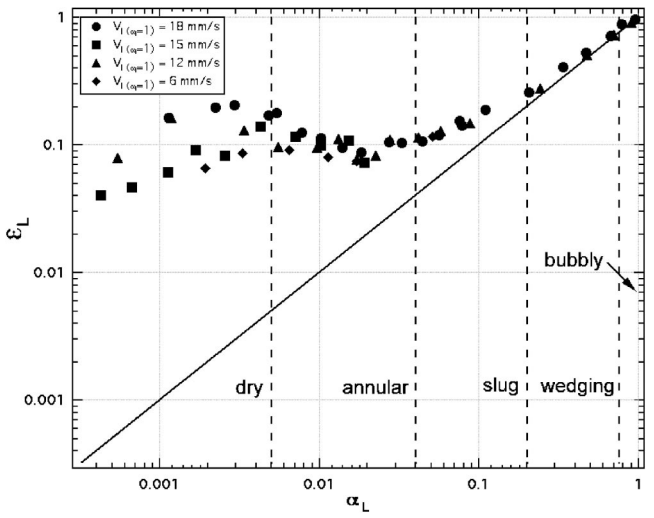

FIG. 8. Apparent liquid fraction ε_L vs homogeneous liquid fraction α_L for different initial conditions (h=525 μm).

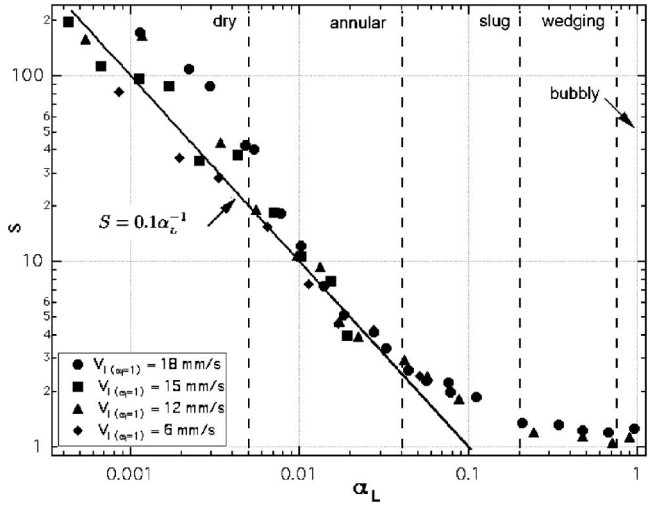

FIG. 9. Slip ratio S between gas and liquid as a function of α_L for different initial conditions (h=525 μm).

Figure 9 shows the slip ratio S as a function of the homogeneous liquid fraction α_L. For the annular and the dry flow, experimental data suggest a relationship as

$$S = 0.1\alpha_L^{-1}. \tag{6}$$

The large slip between the two phases can be attributed to wall shear for the liquid, while the gas can flow unhindered in the channel core. S is meaningless for $\alpha_L = 0$. In a 100 μm circular channel, Kawahara *et al.*[16] reported a large slip ratio S compared to macrochannels and minichannels. For example, they found $S \approx 16$ for $\alpha_L \approx 0.2$. In our case, the combined effect of noncircular capillaries and microsize channels dramatically enhances the slip ratio between liquid and gas.

V. FLOW PATTERNS

A. Bubbly flow

In bubbly flow [Fig. 4(a)], the gas phase is distributed as discrete spherical bubbles in a continuous liquid phase. The bubble size d is smaller than the channel height h. As individual bubbles may collide and coalesce to form large bubbles, polydispersity is observed. For low liquid velocities J_L, some bubbles adhere to the walls. The detachment of a bubble involves two forces, the drag force and the adhesion force. Experiments in slit microchannels related a critical bubble size to a critical capillary number for the bubble to detach for given receding and advancing contact angles.[27] As the flow inside a square channel is nonaxisymmetric close to the walls,[26] and is modified by the presence of bubbles, different bubble sizes are trapped and released from the surface showing a random behavior. To observe the flow path around the bubbles, experiments were preformed adding latex beads (4 μm) to the liquid. It has been found that bubbles pinned on the walls were actually spinning.

Specific to that flow regime, the bubble motion is dependent upon the channel orientation with respect to the gravity when $d \ll h$. The presented experiments were performed with horizontal channels. For low liquid velocity, bubble clogging

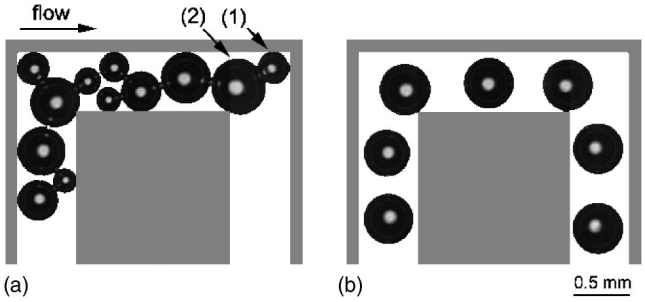

FIG. 10. Bubbly flow: effect of a sharp return; (a) low liquid velocity, (b) high liquid velocity.

occurs in sharp corner bends [Fig. 10(a)]. As the liquid flow in the vicinity of the corner is very small, a small bubble (1) can easily be trapped; the effective channel size is then reduced and a bubble too large to pass through the corner becomes trapped as well (2). Other bubbles become trapped as a chain reaction until they eventually merge and pass the bend. At higher liquid flow rates, bubbles are not perturbed by the sharp bend [Fig. 10(b)]. This effect can be removed using a curved bend. The bend effect on two-phase flow was investigated in larger channels[28] and has been shown to increase coalescence of small bubbles in some flow conditions. In our experiments, bubble size and velocity were not significantly perturbed by this geometry except for the case discussed above. We note that the bubbly flow is not accessible to the system when a mechanical pump supplies the liquid.

B. Wedging flow

The wedging flow [Fig. 4(b)] consists of elongated bubbles, the size of which d is larger than the channel width h ($d>h$). When the flow is steadily developed ($\alpha_L<0.70$), bubbles are equally spaced and monodisperse. The wedging flow exhibits some differences from the Taylor bubble flow, usually reported in the literature.[15] For a partially wetting system, as a function of the bubble velocity V_B, bubbles can dry out the center of the channel creating triple lines (liquid/gas/solid). The liquid film between the gas and the center of the channel can be considered as static, while liquid flows in the corner. The film thickness δ was shown to depend on the bubble length d.[29] A liquid film of thickness δ is known to be metastable if $\delta<\delta_C$, δ_C being the critical thickness defined by

$$\delta_C = 2\lambda_C \sin\left(\frac{\theta_r}{2}\right), \tag{7}$$

where λ_C is the capillary length $[\lambda_C=(\gamma/g(\rho_L-\rho_G))]^{1/2}$, where g is the gravity and ρ_L and ρ_G are, respectively, the liquid and gas densities). In that case, the film can dewet by nucleation and growth of dry patches when their size is greater than a critical value r_C defined as[30]

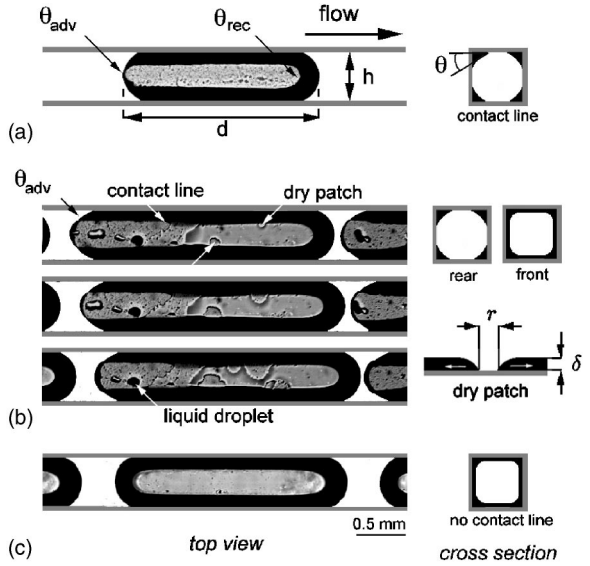

FIG. 11. Wedging flow: (a) drying bubble, (b) consecutive images of a hybrid bubble, and (c) lubricated bubble.

$$r_C = \frac{\delta}{l_r \sin\theta_r}, \tag{8}$$

where l_r is a logarithmic function of r_C. For the capillary regime ($\lambda_C<r_C$), the dewetting velocity U_{dew} is constant and independent of the film thickness,[31]

$$U_{dew} = \frac{U^*\theta^3}{6L_L}, \tag{9}$$

where U^* is the characteristic velocity of the liquid ($U^*=\gamma/\eta$) and L_L is a prefactor depending on the liquid. The dewetting velocity was measured from image processing on glass in the channel and was found to be $U_{dew}\approx 7$ mm/s. Three kinds of wedging bubbles were observed as a function of their velocity V_B (see Fig. 11), which are as follows.

(a) When $V_B<U_{dew}$, bubbles completely dry out the solid surface in the center of the channel. The contact angle at the front of the bubble is the receding contact angle θ_r and the one at the rear of the bubble is the advancing contact angle θ_a.

(b) When $U_{dew}<V_B<V_C$, bubbles present complex contact lines. The front of the bubble is lubricated because dry patches grow slower than the bubble speed. There is no contact angle at the front of the bubble. V_C is the critical bubble velocity for the center of the channel at rear of the bubble to be dried out ($V_C\approx U_{dew}d/h$). At the rear of the bubble, the contact angle is still the advancing contact angle θ_a.

(c) When $V_C<V_B$, bubbles are lubricated by a thin liquid film and there is no contact line.

Dry patches can start from the contact line close to the center of the walls but also directly from the film suggesting that heterogeneities can start the process. A few studies have been conducted on the shape of a dewetting contact line.[32,33]

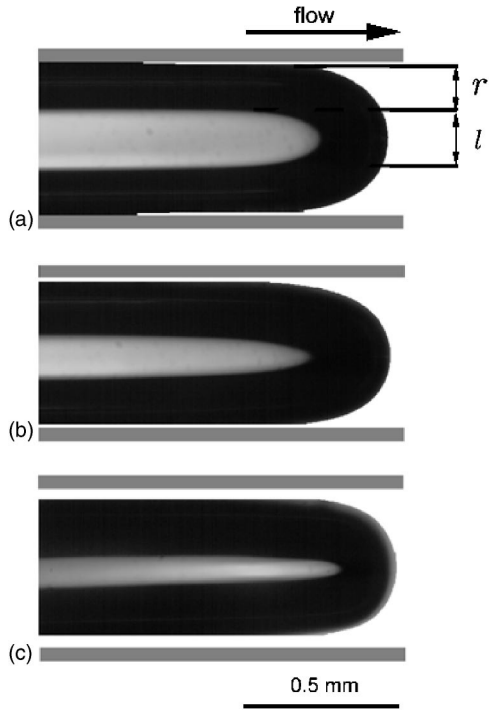

FIG. 12. Slug flow: bubble noses for different capillary numbers; (a) Ca ≈ 0.009, (b) Ca ≈ 0.013, and (c) Ca ≈ 0.018.

C. Slug flow

For $\alpha_L < 0.20$, bubbles distribute themselves in slug [Fig. 4(c)]. The bubble size is far larger than the channel height ($d \gg h$). Bubbles are surrounded by liquid so they do not touch the channel walls. For long bubbles the film between gas and solid may dry out. In a previous investigation, Wong *et al.*[29] demonstrated the decrease of the film thickness δ along the bubble. In some case, growing dry patches were locally observed at the bottom of the gas slug on specific channel locations, suggesting the nucleation was induced by local surface defects.

The nose of the bubbles has a characteristic bullet shape. When a semi-infinite bubble is injected into a liquid filled square capillary, Kolb and Cerro[34] studied the transition from a nonaxisymmetric bubble nose profile to an axisymmetric bubble nose profile for a capillary number of Ca ≈ 0.1. In the case of a bubble-train flow, when liquid is coflowing with gas, Fig. 12 represents the bubble nose profile for different Ca. The radius of curvature of the liquid/gas interface increases while the size of the core gas l diminishes, suggesting a transition from a nonaxisymmetric profile to an axisymmetric profile for a lower Ca. In our experiments, within the range of the liquid and gas flow rates investigated, Ca ≈ 0.1 corresponds to an annular or to a dry flow. The change of the bubble profile affects the apparent liquid fraction ε_L. The apparent liquid fraction does not decrease monotonically with the gas flow rate in our pressurized system, as shown in Sec. IV. An interesting feature of the slug flow is the recirculating liquid flow between bubbles, leading to different degrees of mixing, as a function of Ca.[10,35]

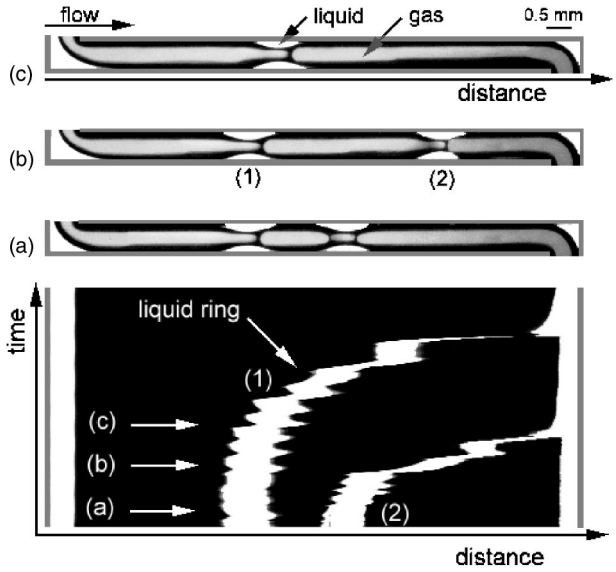

FIG. 13. Annular flow: time-space diagram of liquid ring motion along the gas core.

D. Annular flow

As the liquid fraction α_L decreases, the size of the bubbles increases until the bubble size is equal to the channel length ($d = L$); the flow becomes then annular [see Fig. 4(d)]. In that situation, a continuous central gas core is surrounded by liquid. As in larger channels,[36] interfacial waves along the gas core were observed. This flow regime is known to be rather complex because of transient phenomena depending on the nature of the waves (ripples, flooding, and disturbance waves). In square microchannels, because of the importance of capillary effects, no droplets entrainment, i.e., mist flow was observed over the range of flow rates investigated. Waves are composed of liquid rings traveling along the gas core. Figure 13 shows an example of complex wave propagation. A time-space diagram was created along part of the channel; pictures (a), (b), and (c) represent different times as indicated on the diagram. The waves oscillate, they can go upstream and their random motion does not suggest any correlation between them [wave (2) is moving away from wave (1)]. Liquid rings can grow and disappear from the flow inside the channel.

As in triangular geometry,[23] as α_L decreases, pressure fluctuations decrease. However, the mean pressure inside the channel is constant for given liquid and gas flow rates. The wave velocity is largely slower than the gas motion. As a gas cylinder is highly unstable compared to a liquid cylinder,[37] further work is required to understand those phenomena.

E. Dry flow

When $\alpha_G > 0.995$, the gas core becomes more and more steady. Waves disappear and the liquid is only transported on the wedges. The liquid film thickness decreases until the stability limit is reached so dry patches can grow. When the film dries out, as a result of dewetting processes, liquid droplets

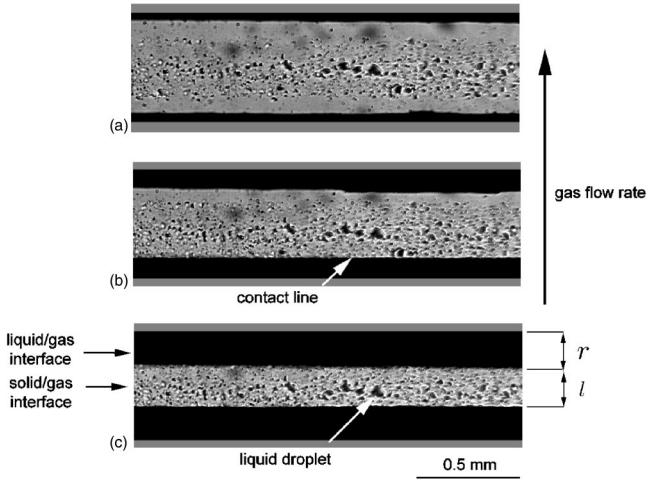

FIG. 14. Dry flow: the central gas core dries out the center of channel walls.

stay on the solid wall (see Fig. 14). The radial size of the gas/solid contact l increases with the gas flow rate Q_G, as α_L decreases. Single gas flow occurs when $l=h$.

VI. PRESSURE DROP

Pressure drop caused by frictional force in two-phase flow is a parameter of prime interest to determine the conditions for the flow. A typical plot of the pressure drop as a function of the capillary number $\mathrm{Ca}=\eta_L J/\gamma$ is shown in Fig. 15. Each flow regime has a different dependence on Ca, except for the bubbly and the wedging flow. On the other hand, when ΔP is plotted versus the gas superficial velocity [Fig. 15 (right)], the transition between bubbly and wedging flows appears clearly. The transition from the wedging to the slug flow causes a large drop in pressure. At the same gas inlet and liquid inlet pressure, the system switches from one regime to another. The slug flow presents an interesting feature of decay of pressure with gas flow rate. Ratulowski and Chang[11] proposed an expression for the pressure, assuming

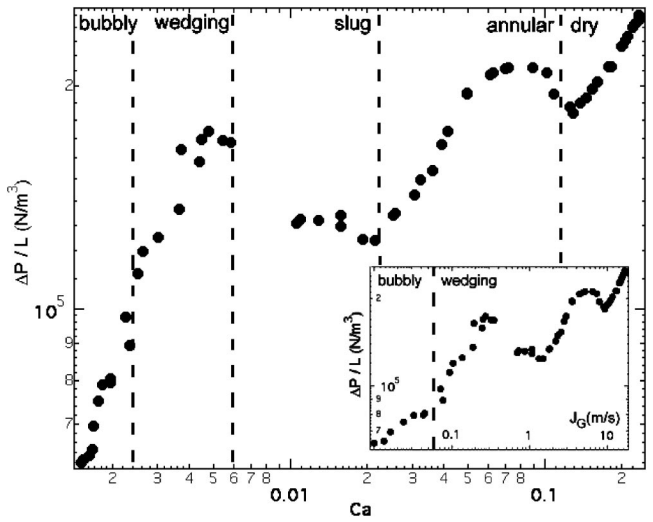

FIG. 15. Typical pressure drop measurement ΔP as a function of the capillary number Ca ($h=200$ μm). Transitions between flow regimes cause a change on the pressure drop dependence on Ca and J_G.

that the pressure drop is the sum of the pressure across bubbles and liquid slugs. They found an expression for the pressure that is proportional to the number of bubbles in the channel nb. As nb is decreasing with the gas flow rate for a given channel of length L, the pressure drop decreases for the slug flow. For the annular flow, the presence of a maximum in the pressure gradient was observed in larger channels[36] and it was attributed to a transition from a mist flow to an annular flow. In our case, as the liquid volume fraction α_L decreases, the liquid friction decreases as well. For the dry flow, the effective channel size for the gas flow approaches that of single gas flow and the pressure converges asymptotically to the single gas one.

A. Single-phase flow

For a laminar steady state flow of fluid i in a square channel ($\mathrm{Re}<3000$), the pressure gradient is related to the flow rate as[38]

$$Q_i = \frac{h^4}{A\eta_i}\nabla P, \tag{10}$$

where $A\approx 28.43$ is a numerical constant, h is the channel height, and η_i is the dynamic viscosity of fluid i. Analogous to electrical resistance, fluidic resistance R is defined as the ratio of pressure difference over flow rate.[17] Assuming a constant pressure gradient along the channel of length L and using Eq. (10), fluidic resistance R_i of fluid i can be written as

$$R_i = A\frac{L\eta_i}{h^4}. \tag{11}$$

For the 200 and the 525 μm square channels, the DI water resistance R_L was calculated from 0.01 to 0.5 $\mathrm{cm}^3/\mathrm{min}$, and the air resistance R_G was calculated from 0.01 to 30 $\mathrm{cm}^3/\mathrm{min}$. From pressure measurements, in the 200 μm channels, $R_{L(\mathrm{exp})}/L\approx 1.64\times 10^{13}\ \mathrm{kg\,m^{-5}\,s^{-1}}$ and $R_{G(\mathrm{exp})}/L\approx 3.19\times 10^{11}\ \mathrm{kg\,m^{-6}\,s^{-1}}$. Using Eq. (11) with the uncertainties on the channel sizes, $\Delta h=10$ μm, the calculated resistance values, $R_{L(\mathrm{theo})}/L=(1.78\pm 0.40)10^{13}\ \mathrm{kg\,m^{-5}\,s^{-1}}$ and $R_{G(\mathrm{theo})}/L=(3.23\pm 0.74)10^{11}\ \mathrm{kg\,m^{-5}\,s^{-1}}$, agree well with the measured resistances per unit of length. As well, in the 525 μm channels, experimental resistances, $R_{L(\mathrm{exp})}/L\approx 3.56\times 10^{11}\ \mathrm{kg\,m^{-5}\,s^{-1}}$ and $R_{G(\mathrm{exp})}/L\approx 6.55\times 10^{9}\ \mathrm{kg\,m^{-5}\,s^{-1}}$, are consistent with the resistances calculated using Eq. (11), $R_{L(\mathrm{theo})}/L=(3.74\pm 0.30)10^{11}\ \mathrm{kg\,m^{-5}\,s^{-1}}$ and $R_{G(\mathrm{theo})}/L=(6.81\pm 0.54)10^{9}\ \mathrm{kg\,m^{-5}\,s^{-1}}$.

B. Two-phase flow

Two-phase flow pressure drop is greater than that of single-phase flow. Different models have been proposed to predict the pressure drop across a bubble train in square capillary. Ransohoff and Radke[5] proposed a dimensionless flow resistance $\beta=h^2\ \mathrm{grad}\ P/\eta J$. Ratulowski and Chang[11] correlated the pressure drop to the capillary number: $\Delta P=a\mathrm{Ca}^n$, where a and n are numerical constants depending on the bubble shape (axisymmetric or nonaxisymmetric). Wong *et*

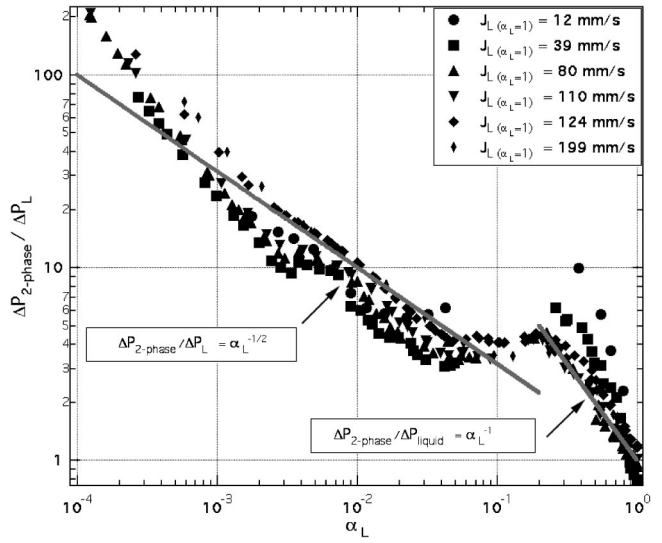

FIG. 16. Two-phase flow pressure drop scaled by single liquid flow pressure drop as a function of homogeneous liquid volume fraction α_L ($h=200$ μm).

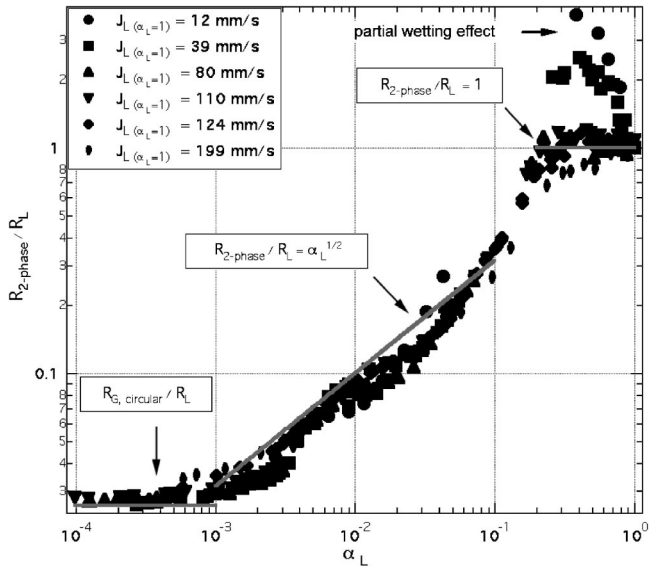

FIG. 17. Two-phase fluidic resistance $R_{2\text{-phase}}$ compared to liquid resistance R_L as a function of homogeneous liquid fraction α_L ($h=200$ μm).

al.[13] took into account the capillary geometry and the bubble length for the pressure-velocity calculation for bubble flow in polygonal capillaries. They found that pressure drop scales linearly with Ca when the liquid bypasses the bubble through corner channels (corner flow) and that it scales with $Ca^{2/3}$ when the liquid is essentially pushing the bubble (plug flow). Stanley *et al.*[12] analyzed their pressure drop data in different square microchannels using the homogeneous flow model with the Fanning equation leading to $f=C/\mathrm{Re}^n$, where f is the friction coefficient, C and n are numerical constants depending on the flow (laminar or turbulent), and Re is the Reynolds number.

Applied to our experimental data these correlations were inaccurate in predicting the measured pressure drops ΔP. This can be attributed to several factors. First, the dependence of the slip ratio S between liquid and gas velocities on the homogeneous liquid fraction α_L [Eq. (6)] hinders the use of an apparent viscosity of the mixture used to calculate the capillary number Ca and the Reynolds number Re. Also, the change in pressure ΔP that is dependent on the average mixture velocity J between the annular and dry flows disables a model that takes into account a monotonical change of the slip ratio S with J. The Lockhart and Martinelli model did not provide good prediction nor transition between flow patterns. This is not surprising as Lockhart-Martinelli correlations are known to provide poor agreement when the flow is laminar.[22]

Since liquid is mostly flowing along the channel walls, the contribution of the liquid viscosity to the frictional pressure drop is predominant. Figure 16 shows the evolution of the pressure drop for 200 μm square channels as a function of the homogeneous liquid fraction α_L. The two-phase pressure drop $\Delta P_{2\text{-phase}}$ was scaled by the single liquid flow pressure drop ΔP_L associated to the liquid flow rate Q_L in the channel ($\Delta P_L = R_L Q_L$). As can be seen in the figure, data collapse more or less on a single master curve with two distinct regimes. The bubbly and the wedging flows are depicted on one side and the slug, annular, and dry flows are on the other side. For the bubbly and the wedging flows, the pressure drop associated can be written as

$$\Delta P_{2\text{-phase}} = \Delta P_L \alpha_L^{-1}. \tag{12}$$

In that case the flow can simply be considered as a single liquid flow with a velocity V corresponding to the mean liquid velocity $V_L = J_L/\alpha_L$. As can be seen in Fig. 16, the deviation to Eq. (12) increases as the liquid velocity decreases (circles and squares) because of wetting phenomena (see wedging flow).

For smaller liquid fraction, the homogeneous model is not realistic because of the slip between the phases. Nevertheless, a simple empirical correlation for the pressure can be written as

$$\Delta P_{2\text{-phase}} = \Delta P_L \alpha_L^{-1/2}. \tag{13}$$

This equation better fits the data for high liquid flow rate.

As α_L changes from 1 to 0, the system goes from a single liquid flow to a single gas flow. The fluidic resistance $R=\Delta P/Q$ is an interesting parameter because it is calculable from direct measurements without assuming any correlation. The two-phase flow fluidic resistance $R_{2\text{-phase}}$ can be defined as

$$R_{2\text{-phase}} = \frac{\Delta P_{2\text{-phase}}}{Q_L + Q_G}. \tag{14}$$

Figure 17 shows the variation of $R_{2\text{-phase}}$ with the homogeneous liquid fraction α_L. For high liquid fractions, using Eq. (12), $R_{2\text{-phase}}$ can be written as

$$R_{2\text{-phase}} = R_L. \tag{15}$$

The deviation for slow liquid velocity appears clearly as contact lines increase the resistance to flow. For low liquid fractions, using Eq. (13), $R_{2\text{-phase}}$ can be written as

$$R_{2\text{-phase}} = R_L \alpha_L^{1/2}. \tag{16}$$

At the transition between the annular and the dry flows, the flow can be seen as a gas flow in a circular tube of diameter h and a liquid flow in the corners. The gas resistance in a circular tube of diameter h is $R_{G,circular} = 128\eta_G L/\pi h^4$. In this situation, assuming that the contribution to the pressure drop is essentially due to the gas flow because of the large slip ratio, the two-phase resistance can be written $R_{2\text{-phase}} \approx R_{G,circular} \approx 0.026 R_L$ for the case of water and air. As can be seen in Fig. 17, the two-phase flow resistance $R_{2\text{-phase}}$ experimentally converges to the calculated circular channel gas resistance $R_{G,circular}$ for $\alpha_L < 10^{-3}$.

VII. SUMMARY

In this paper, we describe experimental conditions used to obtain a steady and homogeneous gas/liquid flow in a microchannel using a cross-shaped section. Bubbles vary in size depending on the flow rates. The two-phase flow map and the transition lines between flow regimes are drawn for 200 and 525 μm square microchannels. Over the range of liquid and gas flow rates investigated, the flow map does not depend on the microchannel size, contrary to large channels. For bubble-train flows, bubble velocity was measured and was found to be equal to the average mixture velocity. The apparent liquid fraction is compared to the homogeneous liquid fraction and the slip ratio between the liquid and the gas velocity is shown to monotonically increase with the void fraction. Flow patterns (bubbly, wedging, slug, annular, and dry flows) and their characteristics are individually detailed. Because of the small channel size, wettability plays an important role in the system. Experiments in partially nonwetting channels ($\theta > 90°$) showed different flow patterns and nonhomogeneous flow along the test channel due to the correlation between the dynamic contact angle and the contact line motion. For partially wetting channels, and when the liquid is flowing in the corners ($\theta < 45°$), wedging and dry flows are described as specific to noncircular capillaries. These flows correspond to local or global dry out of the channel walls by bubbles. The pressure drop is measured from a single liquid flow to a single gas flow for different flow rates. Pressure measurements are correlated to liquid and gas flow rates and show two flow regimes, one in which the liquid is essentially pushing the bubbles and another in which the liquid is flowing in the corners. Taking into account the homogeneous liquid fraction along the channel, and expression for the two-phase hydraulic resistance is experimentally developed over the range of liquid and gas flow rates investigated.

ACKNOWLEDGMENT

This work was supported by DARPA/MTO, "Micro Power Generation" program.

[1] T. J. Yen, X. Zhang, G. Q. Lu, and Y. Wang, "A micro methanol fuel cell operating at near room temperature," Appl. Phys. Lett. **83**, 4056 (2003).
[2] A. M. Barajas and R. L. Panton, "The effect of contact angle on two-phase flow in capillary tubes," Int. J. Multiphase Flow **19**, 337 (1992).
[3] B. Legait, "Laminar flow of two phases through a capillary tube with variable square cross section," J. Colloid Interface Sci. **96**, 28 (1983).
[4] T. C. Ransohoff and C. J. Radke, "Weeping flow around nonwetting bubbles trapped in constricted non circular pores," PCH, PhysicoChem. Hydrodyn. **8**, 255 (1987).
[5] T. C. Ransohoff and C. J. Radke, "Laminar flow of a wetting liquid along the corners of a predominantly gas-occupied noncircular pore," J. Colloid Interface Sci. **121**, 392 (1988).
[6] P. Concus and R. Finn, "On capillary free surfaces in absence of gravity," Acta Math. **132**, 177 (1974).
[7] H. Wong, S. Morris, and C. Radke, "Three-dimensional menisci in polygonal capillaries," J. Colloid Interface Sci. **148**, 317 (1991).
[8] T. Thorsen, R. W. Roberts, F. H. Arnold, and S. R. Quake, "Dynamic pattern formation in a vesicle-generating microfluidic device," Phys. Rev. Lett. **86**, 4163 (2001).
[9] R. Dreyfus, P. Tabeling, and H. Willaime, "Ordered and disordered patterns in two-phase flows in microchannels," Phys. Rev. Lett. **90**, 144505 (2003).
[10] T. Kraus, A. Günther, N. de Mas, M. A. Schmidt, and K. F. Jensen, "An integrated multiphase flow sensor for microchannels," Exp. Fluids **36**, 819 (2004).
[11] J. Ratulowski and H.-C. Chang, "Transport of gas bubbles in capillaries," Phys. Fluids A **1**, 1642 (1989).
[12] R. S. Stanley, R. F. Barron, and T. A. Amee, "Two-phase flow in microchannels," *Mico-electromechanical Systems (MEMS), 1997*, ASME-HTD, Vol. 354 (ASME, New York, 1997).
[13] H. Wong, C. J. Rake, and S. Morris, "The motion of long bubbles in polygonal capillaries. Part 2. Drag, fluid pressure, and fluid flow," J. Fluid Mech. **292**, 95 (1995).
[14] A. F. Akselrod, "Pressure and void fraction pulsations in two-phase flow," *Gas Liquid Flows, 1993*, ASME-FED, Vol. 165 (ASME, New York, 1993).
[15] J. L. Xu, P. Cheng, and T. S. Zhao, "Gas-liquid two-phase flow regimes in rectangular channels with mini/micro gaps," Int. J. Multiphase Flow **25**, 411 (1999).
[16] A. Kawahara, P.-Y. Chung, and M. Kawaji, "Investigation of two-phase flow pattern, void fraction and pressure drop in microchannel," Int. J. Multiphase Flow **28**, 1411 (2002).
[17] G. T. A. Kovacs, *Micromachined Transducers Sourcebook* (McGraw-Hill, New York, 1998).
[18] A. M. Gañán-Calvo and J. M. Gordillo, "Perfectly monodisperse microbubbling by capillary flow focusing," Phys. Rev. Lett. **87**, 274501 (2001).
[19] K. A. Triplett, S. M. Ghiaasiaan, S. Abdel-Khalik, and D. Sadowski, "Gas-liquid two-phase flow in microchannels," Int. J. Multiphase Flow **25**, 337 (1999).
[20] W. L. Chen, M. Twu, and C. Pan, "Gas-liquid two-phase flow in microchannels," Int. J. Multiphase Flow **28**, 1235 (2002).
[21] K. Mishima and T. Hibiki, "Some characteristics of air-water two-phase flow in small diameter vertical tubes," Int. J. Multiphase Flow **22**, 703 (1996).
[22] J. W. Coleman and S. Garimella, "Characterization of two-phase flow patterns in small diameter round and rectangular tubes," Int. J. Heat Mass Transfer **42**, 2869 (1999).
[23] T. S. Zhao and Q. C. Bi, "Co-current air-water two-phase flow patterns in vertical triangular microchannels," Int. J. Multiphase Flow **27**, 765 (2001).
[24] F. P. Bretherton, "The motion of bubbles in tubes," J. Fluid Mech. **10**, 166 (1961).
[25] W. S. Bousman and A. Dukler, "Studies of gas liquid flow in microgravity: Void fraction, pressure drop and flow patterns," *Fluid Mechanics Phenomena in Microgravity, 1993*, ASME-FED, Vol. 175 (ASME, New York, 1993).
[26] W. B. Kolb and R. L. Cerro, "Coating the inside of a capillary of square cross section," Chem. Eng. Sci. **46**, 2181 (1991).
[27] B. Blackmore, D. Li, and J. Gao, "Detachment of bubbles in slit microchannels by shearing flow," J. Colloid Interface Sci. **241**, 514 (2001).
[28] A. Kariyasaki, T. F. Fukano, M. Kagawa, and A. Ousaka, "Air-water two phase flow through a horizontal capillary return bend," *Gas Liquid Flows, 1995*, ASME-FED, Vol. 225 (ASME, New York, 1995).
[29] H. Wong, C. J. Rake, and S. Morris, "The motion of long bubbles in polygonal capillaries. Part 1. Thin films," J. Fluid Mech. **292**, 71 (1995).
[30] C. Sykes, C. Andrieu, V. Détappe, and S. Deniau, "Critical radius of holes in liquid coating," J. Phys. III **4**, 775 (1994).
[31] C. Redon, F. Brochrad-Wyart, and F. Rondelez, "Dynamics of dewetting," Phys. Rev. Lett. **66**, 715 (1991).
[32] T. Cubaud, P. Jenffer, and M. Fermigier, "Dewetting of patterned sur-

faces," Fourth European Coating Symposium, Advances in Coating Processes, edited by J.-M. Buchlin and J. Anthoine (Brussels, 2001).
[33]L. Schwartz, R. V. Roy, R. R. Eley, and S. Petrash, "Dewetting patterns in a drying liquid film," J. Colloid Interface Sci. **234**, 363 (2001).
[34]W. B. Kolb and R. L. Cerro, "The motion of long bubbles in tubes of square cross section," Phys. Fluids A **5**, 1549 (1993).
[35]T. C. Thulasidas, M. Abraham, and R. L. Cerro, "Flow pattern in liquid slugs during bubble-train flow inside capillaries," Chem. Eng. Sci. **52**, 2947 (1997).
[36]G. F. Hewitt and A. H. Govan, "Phenomena and prediction in annular two-phase flow," *Advances in Gas-Liquid Flows, 1990*, ASME-FED, Vol. 99 (ASME, New York, 1990).
[37]J. M. Gordillo, A. M. Gañán-Calvo, and M. Perez-Saborid, "Monodisperse microbubbling: Absolute instabilities in coflowing gas-liquid jets," Phys. Fluids **13**, 3839 (2001).
[38]F. M. White, *Viscous Fluid Flow* (McGraw-Hill, New York, 1991).